

# Chirality and quasi-long-range order in finite-flux Gutzwiller states for magnetized frustrated magnets

Wen O. Wang,<sup>1</sup> Urban F. P. Seifert,<sup>2</sup> Oleg A. Starykh,<sup>3</sup> and Leon Balents<sup>1, 4, 5</sup>

<sup>1</sup>*Kavli Institute for Theoretical Physics, University of California, Santa Barbara, CA 93106-4030, USA*

<sup>2</sup>*Institute for Theoretical Physics, University of Cologne, Zülpicher Str. 77a, 50937 Cologne, Germany*

<sup>3</sup>*Department of Physics and Astronomy, University of Utah, Salt Lake City, UT 84112, USA*

<sup>4</sup>*Canadian Institute for Advanced Research, Toronto, Ontario, Canada*

<sup>5</sup>*French American Center for Theoretical Science,*

*CNRS, KITP, Santa Barbara, CA 93106-4030, USA*

(Dated: January 22, 2026)

We study Gutzwiller-projected wavefunctions for triangular-lattice U(1) Dirac spin liquids in a Zeeman field, where we allow the U(1) gauge field to develop a gauge flux, resulting in (spin-split) spinon Landau levels. We find that at a given magnetization, the optimal candidate state has a finite flux chosen such that the spinon filling lies in a  $|C| = 1$  Landau-level gap: it gives the lowest variational energy and the smallest energy variance within our correlation-matrix reconstruction for local Heisenberg-type models. By symmetry, we argue that the finite gauge flux results in a non-zero (staggered) scalar spin chirality, as also numerically observed, and further find that the  $|C| = 1$  state exhibits dominant quasi-long-ranged  $120^\circ$  magnetic correlations. Studying the next-to-optimal wavefunction with a  $|C| = 2$  Landau-level gap, we observe unusual spin-nematic correlations. Our results may provide guidance for analyzing the magnetic-field response of DSL candidate materials and offer numerical diagnostics that can connect to the underlying theory of spinons coupled to an emergent U(1) gauge field.

**Introduction.**—Quantum spin liquids (QSLs) are exotic phases of quantum magnets which exhibit long-ranged entanglement and fractionalized excitations, described by the deconfined phases of emergent gauge theories [1, 2]. As prototypical examples of strongly-correlated matter beyond Landau’s symmetry-breaking framework, they have attracted wide interest, both due to their fundamental properties, but also possible connections to high- $T_c$  superconductivity, quantum magnetism, and potential applications in quantum information science. While a number of candidate materials have been investigated in recent years, an unambiguous identification and characterization of a QSL is impeded by a scarcity of experimental signatures that can be directly attributed to the presence of an emergent gauge field.

A magnetic field is a natural, experimentally relevant perturbation; the characteristic response of a quantum magnet to a Zeeman field may reveal properties of the zero-field ground state. Thus, motivated by recent experiments suggesting a quantum-disordered ground state in triangular-lattice antiferromagnets [3–7], we here investigate the field-induced states emerging from a U(1) Dirac spin liquid (DSL) as a candidate ground state [8–13]. In the U(1) DSL, gapless fermionic spinons couple to an emergent U(1) gauge field. At low energies, this state is described by compact quantum electrodynamics (QED<sub>3</sub>) in 2+1 dims [11, 14].

Previous mean-field considerations by Ran *et al.* [15] indicate that upon applying a Zeeman field the emergent U(1) gauge field develops a finite gauge flux. As a consequence, the spinon Dirac cones give way to relativistic Landau levels, with a finite magnetization given by the

spin polarization of spinons in the half-filled 0th Landau level. Recent Quantum Monte Carlo simulations of an effectively *non-compact* version of the QED<sub>3</sub> low-energy field theory [16] provide evidence that the field-induced flux phase persists in the presence of gauge fluctuations.

A powerful tool to construct a microscopic wavefunction associated with an (effective) parton description is the Gutzwiller projection technique: here, one starts from a free mean-field wavefunction for fermionic partons and explicitly projects to the physical  $S = 1/2$  Hilbert space. The resulting wavefunction is in general highly non-trivial, but, crucially, observables and matrix elements can be evaluated efficiently using variational Monte Carlo (VMC) techniques [17]. While Gutzwiller-projected wavefunctions may yield competitive variational energies [9, 18, 19] and even constitute exact ground states [20], there is little systematic understanding of the physical properties and signatures of the projected wavefunction for a given spinon ansatz state.

Given the field-induced “chiral flux” state of QED<sub>3</sub>, in this Letter, we systematically construct and characterize corresponding microscopic Gutzwiller-projected wavefunctions for frustrated quantum magnets. Specifically, we consider a class of wavefunctions describing Dirac spinons on the triangular lattice in the presence of an additional uniform gauge flux  $\phi$ , which we take as a variational parameter. We find a finite optimal gauge flux  $\phi$  for a given magnetization  $m \neq 0$ . The corresponding projected wavefunction exhibits a *quasi*-long-ranged  $120^\circ$  order and features a finite scalar spin chirality as an order parameter sensitive to a non-zero gauge flux. Our results are relevant to the magnetic-field response of DSL

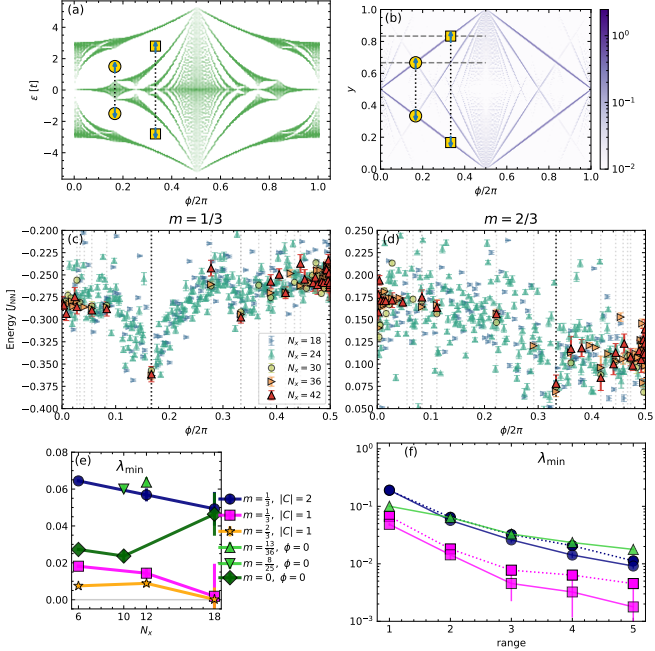


FIG. 1. (a) Hofstadter-butterfly spectrum of the staggered- $\pi$  triangular-lattice spinon Hamiltonian on an  $18 \times 18$  cluster: single-particle energies  $\epsilon$  vs flux density  $\phi/2\pi$ . (b) Corresponding Wannier diagram, where the vertical axis denotes the normalized state index (cumulative filling)  $y$  and the color scale encodes the size of the energy gap between adjacent levels. For rational flux  $\phi/2\pi$ ,  $y$  of each gap obeys  $y = C(\phi/2\pi) + s$  with integer  $C$ , so the slope of each straight line equals the Chern number  $C$  of that gap. The circles and squares mark two  $C = \pm 1$  gaps, where the spin-up and spin-down spinon Fermi levels lie at magnetizations  $m = 1/3$  and  $2/3$ , realized at  $\phi = \pi/3$  and  $2\pi/3$ , respectively. (c,d) Variational energies per site of Eq. 1 as a function of  $\phi$  at magnetizations  $m = 1/3$  and  $2/3$ , respectively. Symbols denote the linear system size ( $N_x = N_y$ ). Vertical dashed lines mark gap-opening fluxes with the smallest nonzero  $|C|$  (notably  $|C| = 1$ ). For  $N_x < 30$  we sample all commensurate fluxes satisfying close-shell conditions, whereas for  $N_x \geq 30$  we restrict to fluxes where the spinon Fermi level lies inside a well-defined Chern gap. (e) Minimal fluctuation eigenvalue  $\lambda_{\min}$  obtained when only range-2 couplings are included. (f)  $\lambda_{\min}$  as a function of the maximum coupling range for the Fermi-pocket state and for the  $|C| = 1,2$  Landau-level states. Dotted (solid) lines correspond to  $6 \times 6$  ( $12 \times 12$ ) lattices.

candidate materials and may be used to infer signatures of an underlying  $\text{QED}_3$  theory of spinons coupled to an emergent gauge field.

*Choice of optimal flux.*—We first construct Gutzwiller-projected wavefunctions via an auxiliary free-fermion spinon Hamiltonian and find the optimal value of the flux per plaquette  $\phi$  (we provide details on Gutzwiller-projected wavefunctions in the End Matter). For a Heisenberg-type system of  $S = 1/2$  in a magnetic field, the total magnetization is a good quantum number: we consider variational states at a fixed magnetization den-

sity  $m = (NS)^{-1} \sum_i S_i^z$  where  $N$  is the number of sites.

For  $m = 0$ , the staggered- $\pi$  flux ansatz with zero net flux provides a competitive approximation to the ground state of the triangular-lattice  $J_1$ - $J_2$  model, even in the absence of (variational) tuning parameters [9, 19, 21, 22]. This flux-free state can be extended to support a finite magnetization  $m > 0$  if the spin-up and spin-down Fermi levels are moved above and below the spinon Dirac nodes, respectively, resulting in *Fermi pockets*. However, upon adding a uniform flux, *Chern gaps* may open in the spinon spectrum – analogous to the gaps between Landau levels – which lower the system’s energy, as found in mean-field and Quantum Monte Carlo studies of the  $\text{QED}_3$  [15, 16]. A priori, the value of  $\phi$  is arbitrary and defines a one-parameter family of wavefunctions at fixed  $m$ . What is the (energetically) optimal choice? To this end, we first investigate the spectrum of the auxiliary spinon Hamiltonian as a function of  $\phi$ , shown in Figs. 1(a,b). The largest topological gaps have  $|C| = 1$ , suggesting that the optimal flux is such that spin-up Fermi level lies in a  $C = +1$  gap and the spin-down Fermi level in the symmetric  $C = -1$  gap about  $\epsilon = 0$ .

To go beyond such a mean-field analysis, we now investigate which choice of  $\phi$  minimizes the variational energy of the corresponding *Gutzwiller-projected* wavefunctions with respect to the nearest-neighbour Heisenberg model

$$H = J_{\text{NN}} \sum_{\langle i,j \rangle} \vec{S}_i \cdot \vec{S}_j. \quad (1)$$

The variational energies are shown as a function of flux  $\phi$  for  $m = 1/3$  and  $2/3$  in Figs. 1(c,d), respectively. We find strong finite-size effects when the Fermi level does not lie inside a well-defined gap; for larger lattices we therefore restrict to flux values where the spinon Fermi level falls within a Chern gap, but noticeable size dependence can persist when the single-particle gap is small.

The “Fermi-pocket” state (with  $\phi = 0$ ) and states in its immediate low-flux vicinity have substantially higher variational energy than states with a sizable flux, where the spinon Fermi level lies inside a Chern gap and the spinons form a gapped “Landau-level” state. The associated lowering of the variational energy is especially pronounced when the Fermi level lies in the largest  $|C| = 1$  gap, and, within statistical and finite-size uncertainties, the corresponding  $|C| = 1$  states yield the lowest variational energies. We conclude that they are the energetically most favorable flux configurations at the level of Gutzwiller-projected wavefunctions. This general behavior is robust when including longer-ranged interactions in Eq. (1). In particular, at the strongly frustrated point  $J_{\text{NNN}}/J_{\text{NN}} = 1/8$  a similar flux dependence is observed (see Fig. S2 in [23]).

*Parent Hamiltonian search.*—To further examine the extent to which these states admit (quasi-)local parent Hamiltonians, we search for such Hamiltonians using the

correlation-matrix method [24]. In this approach, we restrict to the operator set

$$\hat{O}_m \equiv \sum_{\langle ij \rangle_m} \vec{S}_i \cdot \vec{S}_j, \quad m = 1, \dots, 5, \quad (2)$$

i.e., Heisenberg exchanges up to fifth-neighbor bonds, and consider Hamiltonians of the form

$$H(\gamma) = J_0 \sum_m \gamma_m \hat{O}_m, \quad \|\gamma\|_2 = 1, \quad (3)$$

where  $J_0$  sets an overall energy scale. For a given state  $|\psi\rangle$ , we vary  $\gamma$  to minimize the energy variance (see Sec. VII in the Supp. Mat. [23] for details). For each state we denote the resulting minimal energy variance by  $J_0^2 \lambda_{\min}$ . Because our ansatz space is restricted,  $\lambda_{\min} = 0$  is not generically attainable; instead, we use the magnitude of  $\lambda_{\min}$  as a relative measure of how closely the state can be approximated by a local Heisenberg-type Hamiltonian.

Fig. 1(e) shows the results. When only range-2 couplings (nearest- and next-nearest-neighbor) are included, the Fermi-pocket state and the  $|C| = 2$  Landau-level state have larger  $\lambda_{\min}$  than the  $|C| = 1$  state, consistent with the fact that the latter also has the lowest variational energy. Increasing the magnetization further reduces  $\lambda_{\min}$ , as expected since magnetization suppresses quantum fluctuations. The Hamiltonian corresponding to  $\lambda_{\min}$  yields an estimate of the optimal coupling profile to stabilize the trial state. Notably, within this range-2 truncation, we estimate the optimal  $J_{\text{NNNN}}/J_{\text{NN}}$  for the zero-field  $m = 0$  state (cf. Fig. S8 in [23]) and show that the inferred  $J_{\text{NNNN}}/J_{\text{NN}}$  from the reconstructed parent Hamiltonian broadly agrees with the spin-liquid window obtained in previous VMC, DMRG, and CCM studies [8, 9, 25, 26].

As we extend the range of allowed couplings,  $\lambda_{\min}$  decreases for all states, as in Fig. 1(f), but the behavior remains different: for  $|C| = 1$ ,  $\lambda_{\min}$  becomes small and, within the sizable error bars, is even compatible with zero for a sufficiently large lattice, whereas for  $|C| = 2$  and for the Fermi-pocket state remains clearly finite for all sizes and ranges we probed. The results suggest that, within this restricted setting, it is more practical to target a quasi-local Heisenberg-type Hamiltonian for the  $|C| = 1$  state than for either the  $|C| = 2$  state or the Fermi-pocket state.

*In-plane Néel Order.*— We now investigate experimentally accessible spin correlations in the above-constructed states with a finite field-induced gauge flux  $\phi$ . In the parton picture, these states can be viewed as a quantum Hall phase of the spinons in an emergent magnetic field, with opposite Hall conductivities of  $\uparrow$  and  $\downarrow$ -spinons due to their differential occupation of the spin-split Landau levels. Inserting an additional quantum of this emergent flux can be thought of as a defect of the emergent gauge field

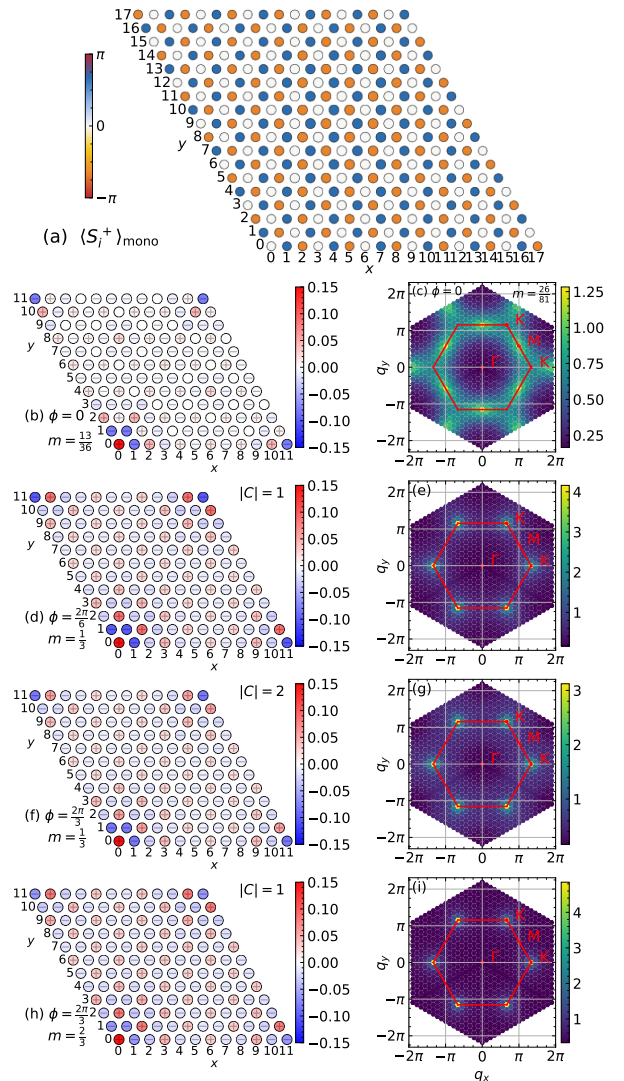


FIG. 2. (a) Monopole matrix element  $\langle S_i^+ \rangle_{\text{mono}}$ , where the color encodes the phase, shown relative to site  $(0,0)$ , and the marker size encodes the magnitude. (b,d,f,h): real-space transverse spin correlator  $C_{ij}^{\perp}$  on  $12 \times 12$  lattices with reference site at  $(0,0)$ . The color scale is clipped to the range  $[-0.15, 0.15]$ ; the on-site value  $C_{00}^{\perp} = 0.5$  lies outside this range and is shown at the saturation color. (c,e,g,i): corresponding momentum-space structure factor  $C^{\perp}(\mathbf{q})$  on  $18 \times 18$  lattices. (b) and (c) have slightly different magnetizations  $m$ , chosen to be the closest available values; the mismatch arises from finite-size closed-shell magnetization levels at different lattice sizes.

in space-time (a “monopole”). Due to the non-trivial topology of spinon wavefunctions in the Landau level state, such a flux defect binds finite spin  $\Delta S^z$  [15, 16, 27]. In a low-energy field theory description, this is reflected by joint monopole-insertion and spin flip  $\langle M_{2\pi}^{\dagger} S^+ \rangle \neq 0$  as a “hidden” order parameter of the flux state [16].

In finite-size systems with torus geometry, a monopole excitation can be constructed by spreading a  $2\pi$  flux

across the lattice [19, 22], so that we may evaluate the order parameter as

$$\langle S_i^+ \rangle_{\text{mono}} \equiv \langle M_{2\pi}^\dagger S_i^+ \rangle \equiv \frac{\langle n+1 | P S_i^+ P | n \rangle}{\langle n | P | n \rangle}, \quad (4)$$

where  $|n\rangle$  is a mean-field Landau-level state with  $n$  flux quanta, and  $P$  denotes the Gutzwiller projection. We adopt the normalization  $\langle n | P | n \rangle$  for our VMC evaluation. In the  $|C| = 1$  Landau-level state, inserting one additional flux quantum pumps an additional state in the  $\uparrow$ - and  $\downarrow$ -spinon bands with  $C = \pm 1$ , respectively. Thus, the net spin pumped is  $\Delta S^z = +1/2 - (-1/2) = +1$ , so  $P|n\rangle$  and  $P|n+1\rangle$  must lie in adjacent  $S^z$  sectors and  $\langle S_i^+ \rangle_{\text{mono}}$  can be nonzero. While in this case, Eq. (4) behaves as an effective transverse spin-1 order-parameter, for  $|C| > 1$ , a monopole binds a spin quantum number of  $\Delta S^z = |C| > 1$  and therefore the corresponding matrix element vanishes. Fig. 2(a) shows the spatial pattern of  $\langle S_i^+ \rangle_{\text{mono}}$  for a  $|C| = 1$  state. The phase of this quantity forms a clear three-sublattice  $120^\circ$  pattern, characteristic of in-plane Néel order on the triangular lattice.

While the monopole matrix element serves as a “hidden” order parameter, we now turn to the real-space transverse spin correlator as an experimentally accessible observable,

$$C_{ij}^\perp \equiv \langle S_i^x S_j^x + S_i^y S_j^y \rangle = \frac{1}{2} \langle S_i^+ S_j^- + S_i^- S_j^+ \rangle \quad (5)$$

and its momentum-space structure factor

$$C^\perp(\mathbf{q}) = \frac{1}{N} \sum_{ij} e^{i\mathbf{q} \cdot (\mathbf{r}_i - \mathbf{r}_j)} C_{ij}^\perp. \quad (6)$$

In Fig. 2(b), we first show  $C_{ij}^\perp$  for the magnetized “Fermi-pocket” state, which is consistent with a collinear anti-ferromagnetic stripe state, and the corresponding structure factor  $C^\perp(\mathbf{q})$  exhibits peaks at the  $M$  points of the Brillouin zone [panel (c)]. For the flux states with magnetization  $m = 1/3$  [close to  $m$  in panels (b,c), cf. Fig. S1 in [23]], we focus on the smallest Chern numbers  $|C| = 1, 2$ , which are associated with two largest spinon gaps: As shown in panels (d-g),  $C_{ij}^\perp$  displays a qualitatively different real-space pattern, consistent with  $120^\circ$  Néel order on the triangular lattice, and  $C^\perp(\mathbf{q})$  develops peaks at the  $K$  points. The nature of these dominant correlations are independent of the system’s magnetization: the  $|C| = 1$  Landau-level state at  $m = 2/3$  in (h,i) likewise shows  $120^\circ$  correlations with  $K$ -point peaks in  $C^\perp(\mathbf{q})$ . Thus, the Fermi-pocket and Landau-level states are distinguished by the leading transverse spin correlations, and this qualitative difference in the spin structure factor could provide an experimentally accessible signature of the Landau-level state.

Note that we observe  $K$ -point in-plane spin correlations not only for  $|C| = 1$  but also for  $|C| = 2$ . However,

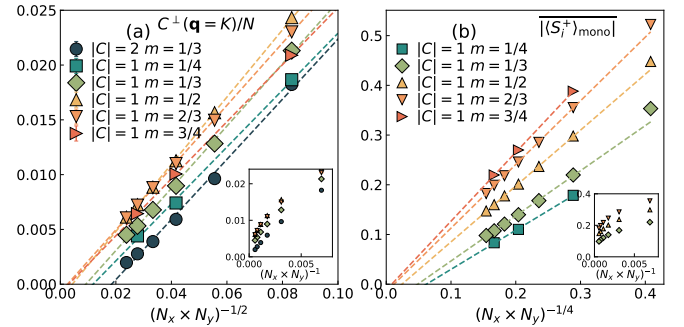


FIG. 3. Finite-size scaling of transverse spin order. (a)  $120^\circ$  order normalized structure factor  $C^\perp(\mathbf{q} = K)/N$  versus  $(N_x \times N_y)^{-1/2}$ . (b) Site-averaged monopole matrix element  $|\langle S_i^+ \rangle_{\text{mono}}|$  versus  $(N_x \times N_y)^{-1/4}$ . Insets show the same data plotted against  $(N_x \times N_y)^{-1}$ . Dashed lines are linear fits using  $N_x = N_y \geq 12$ , shown as guides to the eye.

in the  $|C| = 2$  states,  $120^\circ$  Néel correlations are considerably weaker compared to the  $|C| = 1$  case (see also Fig. S4 in [23]). We argue that these significantly weaker correlations are consistent with the vanishing of the “hidden” order parameter  $\langle S_i^+ \rangle_{\text{mono}} = 0$ .

To probe the nature of in-plane spin correlations at long distances, we perform a finite-size scaling of the structure factor  $C^\perp(\mathbf{q})$  [Fig. 3(a)]. In particular, a divergence  $C^\perp(\mathbf{q}) \sim N$  at some  $\mathbf{q}$ , i.e. a Bragg peak, will signal the formation of off-diagonal long-range order,  $\lim_{|i-j| \rightarrow \infty} C_{ij}^\perp > 0$  in the thermodynamic limit, i.e. spontaneous in-plane magnetic ordering.

The inset of Fig. 3(a) shows that for  $|C| = 2$ ,  $C^\perp(\mathbf{q} = K)/N$  scales approximately linearly with  $N^{-1}$  and extrapolates to zero in the thermodynamic limit. This behavior is consistent with real-space transverse correlations that are summable over distance, i.e., short-ranged (for instance, decaying exponentially or as  $1/r^p$  with  $p > 2$ ). In contrast, for  $|C| = 1$  the data clearly deviate from a simple  $1/N$  scaling: a linear fit in  $N^{-1}$  does not capture the largest system sizes and, if extrapolated, would give an apparent positive intercept, indicating that  $C^\perp(\mathbf{q} = K)/N$  decreases more slowly than  $N^{-1}$ . In the main panel of Fig. 3(a), the  $|C| = 1$  points are much closer to straight lines when plotted versus  $N^{-1/2}$ , though extrapolation gives a slightly negative intercept. This suggests an approximate scaling  $C^\perp(\mathbf{q} = K)/N \propto (N_x N_y)^{-1/2}$ , compatible with a slow algebraic decay  $1/r^p$  with  $p$  likely close to 1 rather than a strictly finite plateau. (See also Fig. S3 in [23] for the logarithmic-scale analysis.) This indicates that the  $|C| = 1$  correlations are more extended than the  $|C| = 2$  state.

It is interesting to compare our analysis of the structure factor with a finite-size scaling of the hidden order parameter  $\langle S_i^+ \rangle_{\text{mono}} = \langle M_{2\pi}^\dagger S_i^+ \rangle$ . In the thermodynamic limit, for the  $|C| = 1$  state, one may expect this to be

related to in-plane long-range order in the spin structure factor: upon inserting a resolution of identity (over all flux sectors) and truncating,  $\lim_{|i-j| \rightarrow \infty} \langle S_i^+ S_j^- + \text{h.c.} \rangle \approx \langle S_i^+ M_{2\pi}^\dagger \rangle \langle M_{2\pi} S_j^- \rangle + \text{h.c.}$  However, we note that a single inserted flux breaks translational symmetry, resulting in a site-dependence of both magnitude and phase of  $\langle S_i^+ \rangle_{\text{mono}}$ , as shown in Fig. 2(a). As the magnitude varies only weakly from site to site, we therefore consider the site-averaged  $|\langle S_i^+ \rangle_{\text{mono}}|$ . In Fig. 3(b), we show the finite-size scaling of  $|\langle S_i^+ \rangle_{\text{mono}}|$ . Notably, in the thermodynamic limit,  $|\langle S_i^+ \rangle_{\text{mono}}| \rightarrow 0$ . The approximately linear behavior in  $(N_x N_y)^{-\frac{1}{4}}$  and strong curvature versus  $(N_x N_y)^{-1}$  in the inset are consistent with the trends in panel (a). Taken together with the finite-size scaling of the structure factor, our results show that the in-plane correlations in the  $|C| = 1$  states are more long-ranged (power-law decaying) than in the short-ranged  $|C| = 2$  state, but we do not find conclusive evidence for genuine long-range order in the thermodynamic limit.

**Scalar Spin Chirality.**—While a magnetic Zeeman field *explicitly* breaks the  $S = 1/2$  time-reversal symmetry  $\mathcal{T} = e^{i\pi S^y} \mathcal{K}$  (here,  $\mathcal{K}$  denotes complex conjugation), the sign of the optimal gauge flux  $\phi \neq 0$  is arbitrary, implying that the wavefunctions under considerations *spontaneously* break another  $\mathbb{Z}_2$  symmetry  $\mathcal{T}' = \mathcal{K}$ . What is an order parameter that resolves this broken symmetry? We examine the scalar chirality

$$\chi_{ijk} \equiv \langle \vec{S}_i \cdot (\vec{S}_j \times \vec{S}_k) \rangle \quad (7)$$

on elementary triangles, a SU(2)-invariant three-spin observable that in principle can be probed experimentally. Fig. 4(a) shows the real-space pattern of  $\chi$  in the projected Landau-level state. The chirality is staggered on up and down triangles (with a uniform magnitude). In the zero-flux state, by contrast, symmetry enforces  $\chi = 0$  (cf. Sec. VIII in [23]). Fig. 4(b) shows that a substantial chirality emerges in the Landau-level states, and its magnitude varies smoothly with  $m$  (and thus with  $\phi$  at fixed  $|C|$ ). The value of  $\chi$  shows minimal size dependence (see Fig. S5 in [23]), indicating that this pattern is robust in the thermodynamic limit.

For comparison, we consider a classical umbrella/cone state of spin-1/2 moments which, similar to the projected  $|C| = 1$  Landau-level state features in-plane  $120^\circ$  order and a finite magnetization due to out-of-plane canting (see Sec. IX in [23]), shown as a function of  $m$  in Fig. 4(b). We find that the chirality in the projected Landau-level state is generally higher than in the classical approximation. To further quantify how “quantum” the chirality is, we also consider the normalized ratio

$$\mathcal{R} \equiv \chi_{ijk} / \left[ \frac{i}{2} \langle S_i^z \rangle \left( \langle S_j^+ S_k^- \rangle - \langle S_j^- S_k^+ \rangle \right. \right. \\ \left. \left. + \langle S_k^+ S_i^- \rangle - \langle S_k^- S_i^+ \rangle + \langle S_i^+ S_j^- \rangle - \langle S_i^- S_j^+ \rangle \right) \right]. \quad (8)$$

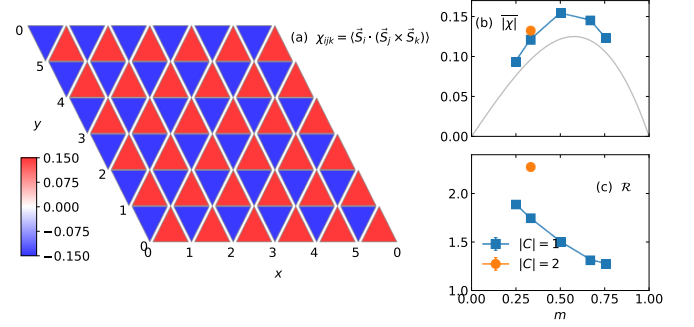


FIG. 4. (a) Scalar spin chirality  $\chi_{ijk} \equiv \langle \vec{S}_i \cdot (\vec{S}_j \times \vec{S}_k) \rangle$  on a  $6 \times 6$  lattice with  $|C| = 1$  and  $m = 2/3$ . (b) Plaquette-averaged magnitude  $|\chi|$  versus magnetization  $m$  on a  $36 \times 36$  lattice. The gray curve shows the classical umbrella-state chirality for reference. (c) Ratio  $\mathcal{R}$  on the same lattice.

(see also Sec. IV in [23]). As shown in Fig. 4(c), this ratio is generically larger than one. This demonstrates sizable connected three-spin correlations beyond a simple factorization into lower-order expectation values, highlighting that the scalar chirality is a genuinely quantum, intrinsic property generated by the spinon gauge flux and Gutzwiller projection, and is finite (and large) even if there is no genuine long-range order present.

**Spin-Nematic Order for  $|C| = 2$ .**—For  $|C| = 2$ , an insertion of  $2\pi$  flux binds a net total spin of  $\Delta S^z = 2$ , as created by an operator of the form  $S_i^+ S_j^+$ , rather than a single  $S_i^+$  as in Eq. (4). We therefore consider possible  $S^+ S^+$  (spin-nematic) order characterized by matrix elements of the form  $\langle S_i^+ S_j^+ \rangle_{\text{mono}} \equiv \langle n + 1 | P S_i^+ S_j^+ P | n \rangle / \langle n | P | n \rangle$ . In principle, this matrix element can be nonzero for any relative displacement between  $i$  and  $j$ , except for the onsite component  $i = j$  which vanishes. Remarkably, we find that the magnitude  $\langle S_i^+ S_j^+ \rangle_{\text{mono}}$  is not maximized at short distances: it grows with separation and approaches a nearly distance-independent plateau at large  $|\mathbf{r}_i - \mathbf{r}_j|$  (see Fig. S6 in [23]). To investigate the spatial structure of this order parameter, we first focus on the simplest, nearest-neighbor pairs. The phase pattern of the nearest-neighbor bond quantity  $\langle S_i^+ S_j^+ \rangle_{\text{mono}}$  is shown in Fig. 5(a). The bonds form a three-sublattice pattern with a  $\sqrt{3} \times \sqrt{3}$ -unit cell, characteristic of  $K$ -point ordering. Consistent with this, the four-spin correlation function  $\langle S_i^+ S_j^+ S_k^- S_l^- \rangle$  exhibits the same three-sublattice structure (see Fig. S7 in [23]).

To investigate this unusual, “unbounded” spin-pair order, we analyze its finite-size scaling behaviour: When plotted versus  $N^{-1}$ , both  $|\langle S_i^+ S_j^+ \rangle_{\text{mono}}|$  and the correlation  $|\langle S_i^+ S_j^+ S_k^- S_l^- + S_i^- S_j^- S_k^+ S_l^+ \rangle|$  in Fig. 5(b) are well described by straight lines with a finite positive intercept. This is again inconsistent with a simple  $1/N$  scaling expected for short-ranged (summable) correlations and indicates a slower (power-law) decay with sys-

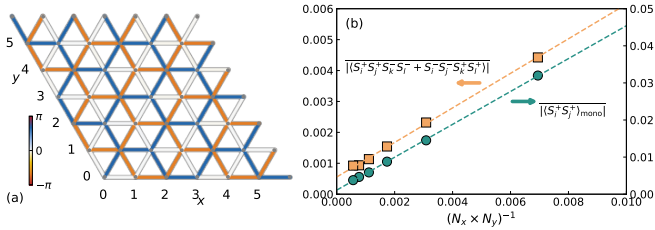


FIG. 5. (a) Phases of the nearest-neighbour monopole matrix element  $\langle S_i^+ S_j^+ \rangle_{\text{mono}}$ , shown relative to the bond  $(i,j) = ((1,0), (0,0))$ . (b) Finite-size scaling of the bond-averaged magnitude of the nearest-neighbour monopole matrix element,  $|\langle S_i^+ S_j^+ \rangle_{\text{mono}}|$ , and of the corresponding four-spin correlator  $|\langle S_i^+ S_j^+ S_k^- S_l^- + S_i^- S_j^- S_k^+ S_l^+ \rangle|$ , which serves as a analogue of a structure factor normalized by  $N$ . Dashed lines are linear fits.

tem size. Within the range of sizes we can access, the data are compatible with two scenarios: either a nonzero thermodynamic-limit value corresponding to long-range nematic order, or a slow algebraic decay with a non-integrable tail that would cause the curves to bend downward only at larger sizes than we can currently reach. Our data do not distinguish these possibilities, but in either case they imply nematic correlations that are more extended than in a short-ranged state, which may be related to the “unbounded” real-space behavior discussed above. Our finite-size scaling of the site-averaged nearest-neighbor  $|\langle S_i^+ S_j^+ \rangle|$  leads to consistent conclusions. While appearing more challenging to realize than the  $|C| = 1$  Landau-level state, as suggested by the variational-energy comparison and the correlation-matrix analysis above, the projected  $|C| = 2$  state exhibits spin-nematic order that merits further study.

*Summary.*—We studied a family of Gutzwiller-projected spinon wavefunctions with non-trivial gauge flux as variational states for magnetized Dirac spin liquids on the triangular lattice. Within this variational setting, the  $|C| = 1$  Landau-level state is favored among the gapped flux candidates we explored: it has the lowest variational energy and the smallest energy variance in our correlation-matrix reconstruction, suggesting that it lies closest to a quasi-local Heisenberg-type parent Hamiltonian. Motivated by this, we characterized the spin correlations in this state in detail. For the  $|C| = 1$  state, extensive finite-size scaling analysis points to slowly decaying, likely algebraic, in-plane antiferromagnetic  $120^\circ$ -type correlations. We further find that the projected wavefunctions feature a staggered scalar spin chirality (on elementary triangles) which may be viewed as an order parameter for a  $\mathbb{Z}_2$  symmetry which is broken spontaneously by a finite gauge flux  $\phi \neq 0$ . The observed correlations are similar to those of a non-coplanar cone/umbrella state of magnetic moments on the triangular lattice (though we stress that we do not find evidence

for genuine long-range antiferromagnetic order), which may be attributed to the presence of a uniform gauge flux – this is in stark contrast to semiclassical studies of triangular lattice Heisenberg antiferromagnets in a field which consistently find coplanar (non-chiral) Y-states [28, 29].

Studying projected wavefunctions associated within the  $|C| = 2$  sector, we observe higher-rank magnetic ordering tendencies, where the leading order parameter is a spin-nematic pattern in  $\langle S_i^+ S_j^+ \rangle$  with an unusual “unbounded” real-space behavior. How such a state might be realized in realistic microscopic models is an interesting question for further studies.

Taken together, our results shed light on properties of a large class of Gutzwiller-projected wavefunctions which support a finite magnetization via the formation of spinon Chern gaps. They may help to motivate and interpret future numerical and experimental searches for the physics of magnetized Dirac spin liquids, in particular the formation of emergent gauge fluxes, in triangular-lattice materials.

*Note added.*—During the preparation of this manuscript, an independent study [30] has reported VMC results for the triangular lattice antiferromagnet in a Zeeman field, where in the vicinity to a zero-field DSL the  $|C| = 1$  flux state is found to energetically outcompete semiclassical (coplanar) ordered states.

*Acknowledgements.*—We gratefully acknowledge discussions with F. Becca, T. Cookmeyer, M. P. A. Fisher, A. Keselman, E. König, J. Knolle, A. Rosch, C. Xu, and J.-X. Zhang. This work is funded by the Deutsche Forschungsgemeinschaft (DFG, German Research Foundation) through SFB 1238, project id 277146847 (UFPS), and the Emmy Noether Program, project id 544397233, SE 3196/2-1 (UFPS). LB is supported by the NSF CMMT program under Grant No. DMR-2419871, and the Simons Collaboration on Ultra-Quantum Matter, which is a grant from the Simons Foundation (Grant No. 651440). WOW acknowledges support from the Gordon and Betty Moore Foundation through Grant GBMF8690 to the University of California, Santa Barbara, to the Kavli Institute for Theoretical Physics (KITP). This research was supported in part by grant NSF PHY-2309135 to the KITP. Simulations made use of computational facilities purchased with funds from the NSF (CNS-1725797) and administered by the Center for Scientific Computing (CSC). The C.S.C. is supported by the California NanoSystems Institute and the Materials Research Science and Engineering Center (MRSEC; NSF DMR 2308708) at UC Santa Barbara.

*Data Availability.*—The data and plotting code needed to reproduce the figures are available at <https://doi.org/10.5281/zenodo.1828318>.

---

[1] L. Savary and L. Balents, Quantum spin liquids: a review, *Reports on Progress in Physics* **80**, 016502 (2016).

[2] J. Knolle and R. Moessner, A field guide to spin liquids, *Annual Review of Condensed Matter Physics* **10**, 451 (2019).

[3] T. Xie, A. A. Eberharter, J. Xing, S. Nishimoto, M. Brando, P. Khanenko, J. Sichelschmidt, A. A. Turrini, D. G. Mazzone, P. G. Naumov, L. D. Sanjeeva, N. Harrison, A. S. Sefat, B. Normand, A. M. Läuchli, A. Podlesnyak, and S. E. Nikitin, Complete field-induced spectral response of the spin-1/2 triangular-lattice antiferromagnet  $\text{csybse}_2$ , *npj Quantum Materials* **8**, 48 (2023).

[4] R. Bag, S. Xu, N. E. Sherman, L. Yadav, A. I. Kolesnikov, A. A. Podlesnyak, E. S. Choi, I. da Silva, J. E. Moore, and S. Haravifard, Evidence of dirac quantum spin liquid in  $\text{ybzn}_2\text{gao}_5$ , *Phys. Rev. Lett.* **133**, 266703 (2024).

[5] A. O. Scheie, E. A. Ghioldi, J. Xing, J. A. M. Paddison, N. E. Sherman, M. Dupont, L. D. Sanjeeva, S. Lee, A. J. Woods, D. Abernathy, D. M. Pajerowski, T. J. Williams, S.-S. Zhang, L. O. Manuel, A. E. Trumper, C. D. Pemmaraju, A. S. Sefat, D. S. Parker, T. P. Devreux, R. Movshovich, J. E. Moore, C. D. Batista, and D. A. Tennant, Proximate spin liquid and fractionalization in the triangular antiferromagnet  $\text{kybse}_2$ , *Nature Physics* **20**, 74 (2024).

[6] A. O. Scheie, M. Lee, K. Wang, P. Laurell, E. S. Choi, D. Pajerowski, Q. Zhang, J. Ma, H. D. Zhou, S. Lee, S. M. Thomas, M. O. Ajeesh, P. F. S. Rosa, A. Chen, V. S. Zapf, M. Heyl, C. D. Batista, E. Dagotto, J. E. Moore, and D. A. Tennant, *Spectrum and low-energy gap in triangular quantum spin liquid naybse<sub>2</sub>* (2024), arXiv:2406.17773 [cond-mat.str-el].

[7] H. C. H. Wu, F. L. Pratt, B. M. Huddart, D. Chatterjee, P. A. Goddard, J. Singleton, D. Prabhakaran, and S. J. Blundell, Spin dynamics in the dirac  $u(1)$  spin liquid  $\text{ybzn}_2\text{gao}_5$ , *Phys. Rev. Lett.* **135**, 046704 (2025).

[8] W.-J. Hu, S.-S. Gong, W. Zhu, and D. N. Sheng, Competing spin-liquid states in the spin- $\frac{1}{2}$  heisenberg model on the triangular lattice, *Phys. Rev. B* **92**, 140403 (2015).

[9] Y. Iqbal, W.-J. Hu, R. Thomale, D. Poilblanc, and F. Becca, Spin liquid nature in the heisenberg  $J_1 - J_2$  triangular antiferromagnet, *Phys. Rev. B* **93**, 144411 (2016).

[10] S. Hu, W. Zhu, S. Eggert, and Y.-C. He, Dirac spin liquid on the spin-1/2 triangular heisenberg antiferromagnet, *Phys. Rev. Lett.* **123**, 207203 (2019).

[11] X.-Y. Song, C. Wang, A. Vishwanath, and Y.-C. He, Unifying description of competing orders in two-dimensional quantum magnets, *Nature Communications* **10**, 4254 (2019).

[12] N. E. Sherman, M. Dupont, and J. E. Moore, Spectral function of the  $J_1 - J_2$  heisenberg model on the triangular lattice, *Phys. Rev. B* **107**, 165146 (2023).

[13] M. Drescher, L. Vanderstraeten, R. Moessner, and F. Pollmann, Dynamical signatures of symmetry-broken and liquid phases in an  $s = \frac{1}{2}$  heisenberg antiferromagnet on the triangular lattice, *Phys. Rev. B* **108**, L220401 (2023).

[14] M. Hermele, T. Senthil, and M. P. A. Fisher, Algebraic spin liquid as the mother of many competing orders, *Phys. Rev. B* **72**, 104404 (2005).

[15] Y. Ran, W.-H. Ko, P. A. Lee, and X.-G. Wen, Spontaneous spin ordering of a dirac spin liquid in a magnetic field, *Phys. Rev. Lett.* **102**, 047205 (2009).

[16] C. Chen, U. F. P. Seifert, K. Feng, O. A. Starykh, L. Balents, and Z. Y. Meng, *Emergent gauge flux in qed<sub>3</sub> with flavor chemical potential: application to magnetized u(1) dirac spin liquids* (2025), arXiv:2508.08528 [cond-mat.str-el].

[17] F. Becca and S. Sorella, Quantum monte carlo approaches for correlated systems (Cambridge University Press, Cambridge, 2017).

[18] Y. Iqbal, F. Ferrari, A. Chauhan, A. Parola, D. Poilblanc, and F. Becca, Gutzwiller projected states for the  $J_1 - J_2$  heisenberg model on the kagome lattice: Achievements and pitfalls, *Phys. Rev. B* **104**, 144406 (2021).

[19] A. Wietek, S. Capponi, and A. M. Läuchli, Quantum electrodynamics in 2 + 1 dimensions as the organizing principle of a triangular lattice antiferromagnet, *Phys. Rev. X* **14**, 021010 (2024).

[20] B. S. Shastry, Exact solution of an  $s=1/2$  heisenberg antiferromagnetic chain with long-ranged interactions, *Phys. Rev. Lett.* **60**, 639 (1988).

[21] F. Ferrari and F. Becca, Dynamical structure factor of the  $J_1 - J_2$  heisenberg model on the triangular lattice: Magnons, spinons, and gauge fields, *Phys. Rev. X* **9**, 031026 (2019).

[22] S. Budaraju, A. Parola, Y. Iqbal, F. Becca, and D. Poilblanc, Monopole excitations in the  $u(1)$  dirac spin liquid on the triangular lattice, *Phys. Rev. B* **111**, 125150 (2025).

[23] See the supplemental material for more details.

[24] X.-L. Qi and D. Ranard, Determining a local Hamiltonian from a single eigenstate, *Quantum* **3**, 159 (2019).

[25] Z. Zhu and S. R. White, Spin liquid phase of the  $s = \frac{1}{2} J_1 - J_2$  heisenberg model on the triangular lattice, *Phys. Rev. B* **92**, 041105 (2015).

[26] P. H. Y. Li, R. F. Bishop, and C. E. Campbell, Quasiclassical magnetic order and its loss in a spin- $\frac{1}{2}$  heisenberg antiferromagnet on a triangular lattice with competing bonds, *Phys. Rev. B* **91**, 014426 (2015).

[27] F. Paoletti, D. Guerci, G. Sangiovanni, U. F. P. Seifert, and E. J. König, *Topologically enabled superconductivity: possible implications for rhombohedral graphene* (2025), arXiv:2504.13166 [cond-mat.str-el].

[28] M. Ye and A. V. Chubukov, Quantum phase transitions in the heisenberg  $J_1 - J_2$  triangular antiferromagnet in a magnetic field, *Phys. Rev. B* **95**, 014425 (2017).

[29] A. Keselman, X. Xu, H. Zhang, C. D. Batista, and O. A. Starykh,  *$j_1 - j_2$  triangular lattice antiferromagnet in a magnetic field* (2025), arXiv:2512.02150 [cond-mat.str-el].

[30] T. Bader, S. Feng, S. Budaraju, F. Becca, J. Knolle, and F. Pollmann, *Triangular  $j_1-j_2$  heisenberg antiferromagnet in a magnetic field* (2025), arXiv:2512.08768 [cond-mat.str-el].

## End Matter

*Gutzwiller-projected wavefunctions.*—We construct Gutzwiller-projected wavefunctions via an auxiliary spinon Hamiltonian

$$H = \sum_{\sigma=\uparrow,\downarrow} \sum_{ij} t_{ij} f_{i,\sigma}^\dagger f_{j,\sigma} + \text{h.c.} \quad (9)$$

Here, the  $t_{ij}$  are complex hopping amplitudes that define an *ansatz*, and in particular also encode the flux experienced by the spinons. For simplicity, we focus on a nearest-neighbor ansatz and fix the amplitude  $|t_{ij}| = |t|$ .

We take the staggered- $(\pi, 0)$  spinon ansatz as our starting point for the unmagnetized Dirac spin liquid (DSL), i.e., in the absence of a Zeeman field. For constructing the Landau-level states, we introduce a uniform orbital magnetic field by attaching additional Peierls phases  $\varphi_{ij}$  to the nearest-neighbor hoppings on the triangular lattice, so that  $t_{ij} \rightarrow t_{ij} e^{i\varphi_{ij}}$ . In this work we define  $\phi$  as the total U(1) flux through a primitive rhombic unit cell of the triangular lattice, i.e. the oriented sum of link phases around the boundary of any such unit cell satisfies

$$\sum_{\langle ij \rangle \in \diamond} \varphi_{ij} = \phi \pmod{2\pi}. \quad (10)$$

Since each primitive rhombic unit cell contains two elementary triangular plaquettes, the corresponding flux per triangle is  $\Phi \equiv \phi/2$ .

The free-fermion Hamiltonian  $H$  is readily diagonalized for a system of  $N$  sites, yielding  $2N$  single-particle wavefunctions. A Slater determinant  $|\psi_f\rangle$  at magnetization  $M$  is obtained by filling the  $N_\uparrow = (N + M)/2$  and  $N_\downarrow = (N - M)/2$  lowest-energy orbitals for spin-up and -down spinons, respectively. Therefore, we occupy  $N$  spinon states in total – i.e., half filling (one spinon per site). We further define  $m = M/N$  as the intensive magnetization. Unless stated otherwise, magnetization values are reported in terms of  $m$ .

A variational wavefunction for the spin-1/2 moments on the triangular lattice is obtained by projecting the Slater determinant  $|\psi_f\rangle$  onto the subspace of single-occupied sites,  $f_{i,\uparrow}^\dagger f_{i,\uparrow} + f_{i,\downarrow}^\dagger f_{i,\downarrow} = 1 \forall i$ . While explicitly constructing (and storing) the projected wavefunction  $P|\psi_f\rangle$  is only feasible for small systems, *observables* with respect to  $P|\psi_f\rangle$  can be efficiently evaluated using Monte Carlo methods [17].

## Supplementary Materials

### I. Implementing Overall Flux

There are different ways to assign Peierls phases  $\varphi_{ij}$  to the bonds. For a fixed flux pattern, different assignments correspond to different gauge choices of the vector potential  $\mathbf{A}$ , and are therefore physically equivalent: they yield the same accumulated phase around any closed loop. A convenient general construction is

$$\varphi_{ij} = \int_{\mathbf{r}_i}^{\mathbf{r}_j} \mathbf{A}(\mathbf{r}) \cdot d\ell, \quad (\text{S1})$$

where  $\mathbf{r}_i = (r_{ix}, r_{iy})$  is the position of site  $i$ , and the line integral is taken along the straight-line segment connecting  $\mathbf{r}_i$  and  $\mathbf{r}_j$ . For simplicity, we work in units where we absorb the factor  $e/\hbar$  into  $\mathbf{A}$ . We choose a vector potential  $\mathbf{A}$  of the form

$$\mathbf{A}(\mathbf{r}) = B \begin{bmatrix} -\alpha r_y \\ (1-\alpha)r_x \end{bmatrix}, \quad (\text{S2})$$

where  $\alpha \in \mathbb{R}$  parametrizes a family of gauges that all produce the same uniform magnetic field. To verify this, note that in two spatial directions the out-of-plane curl is

$$(\nabla \times \mathbf{A})_z = \partial_x A_y - \partial_y A_x = B, \quad (\text{S3})$$

i.e.

$$\nabla \times \mathbf{A}(\mathbf{r}) = B \hat{\mathbf{z}}. \quad (\text{S4})$$

Using Stokes' theorem, the left-hand side of Eq. (10) can be written as a line integral of  $\mathbf{A}$ ,

$$\sum_{\langle ij \rangle \in \diamond} \varphi_{ij} = \oint_{\partial \diamond} \mathbf{A} \cdot d\ell = \iint_{\diamond} (\nabla \times \mathbf{A}) \cdot \hat{\mathbf{z}} d^2 r = B A_{\text{uc}}, \quad (\text{S5})$$

so that the flux through the primitive rhombic unit cell is

$$\phi \equiv B A_{\text{uc}} \pmod{2\pi}. \quad (\text{S6})$$

For a triangular lattice with lattice constant set to  $a = 1$ , the area of the primitive rhombus is  $A_{\text{uc}} = \frac{\sqrt{3}}{2}$ .

On a finite cluster with periodic boundary conditions (a torus), the total U(1) flux piercing the system must be quantized in units of  $2\pi$ . The system contains  $N$  primitive unit cells, so

$$N \phi = 2\pi n, \quad n \in \mathbb{Z}, \quad (\text{S7})$$

which implies that the flux per primitive unit cell can only take the discrete values

$$\phi = \frac{2\pi}{N} n, \quad n = 0, 1, \dots, N-1. \quad (\text{S8})$$

Combining Eqs. (S8) and (S6) then gives the corresponding allowed values of the uniform field strength,

$$B_n = \frac{\phi}{A_{\text{uc}}} = \frac{4\pi n}{\sqrt{3} N}. \quad (\text{S9})$$

When a nearest-neighbor bond crosses the boundary of a finite cluster with periodic identification, one endpoint of the bond lies outside the chosen fundamental domain. We then map that site back into the cluster by a Bravais translation  $\mathbf{L}$ . Because our  $\mathbf{A}(\mathbf{r})$  in Eq. (S2) is not periodic, this “folding back” generally produces an extra (gauge) phase. Instead of the ordinary boundary conditions, we need a modified boundary condition to ensure that the Hamiltonian on the torus is single-valued and that the prescribed flux (i.e., the accumulated Peierls phase around any closed loop) is unchanged by the choice of representative sites.

From Eq. (S2),

$$\mathbf{A}(\mathbf{r} + \mathbf{L}) - \mathbf{A}(\mathbf{r}) = \mathbf{A}(\mathbf{L}), \quad (\text{S10})$$

and the right-hand side is a constant vector, which can be written as the gradient of a scalar function,

$$\mathbf{A}(\mathbf{r} + \mathbf{L}) = \mathbf{A}(\mathbf{r}) + \nabla \chi_{\mathbf{L}}(\mathbf{r}), \quad \chi_{\mathbf{L}}(\mathbf{r}) = \mathbf{A}(\mathbf{L}) \cdot \mathbf{r}. \quad (\text{S11})$$

Using Eq. (S1), shifting both endpoints by  $\mathbf{L}$  gives

$$\begin{aligned} \varphi_{i+\mathbf{L}, j+\mathbf{L}} &= \int_{\mathbf{r}_i+\mathbf{L}}^{\mathbf{r}_j+\mathbf{L}} \mathbf{A}(\mathbf{r}) \cdot d\ell = \int_{\mathbf{r}_i}^{\mathbf{r}_j} [\mathbf{A}(\mathbf{r} + \mathbf{L})] \cdot d\ell \\ &= \int_{\mathbf{r}_i}^{\mathbf{r}_j} [\mathbf{A}(\mathbf{r}) + \nabla \chi_{\mathbf{L}}(\mathbf{r})] \cdot d\ell \\ &= \varphi_{ij} + \chi_{\mathbf{L}}(\mathbf{r}_j) - \chi_{\mathbf{L}}(\mathbf{r}_i) \pmod{2\pi}. \end{aligned} \quad (\text{S12})$$

On a torus we identify  $i \equiv i + \mathbf{L}$ . Accordingly, the hopping operator associated with a given physical bond must be independent of the chosen representative sites:

$$t e^{i\varphi_{ij}} c_i^\dagger c_j \equiv t e^{i\varphi_{i+\mathbf{L}, j+\mathbf{L}}} c_{i+\mathbf{L}}^\dagger c_{j+\mathbf{L}}. \quad (\text{S13})$$

Substituting Eq. (S12) into Eq. (S13) shows that the extra phase  $\chi_{\mathbf{L}}(\mathbf{r}_j) - \chi_{\mathbf{L}}(\mathbf{r}_i)$  must be absorbed by the fermion operators at the boundary. This leads to the modified boundary condition,

$$c_{i+\mathbf{L}} = e^{-i\chi_{\mathbf{L}}(\mathbf{r}_i)} c_i, \quad \chi_{\mathbf{L}}(\mathbf{r}) = \mathbf{A}(\mathbf{L}) \cdot \mathbf{r}. \quad (\text{S14})$$

Notice that from Eq. (S14) one obtains, by replacing  $i \rightarrow i - \mathbf{L}$ ,

$$c_i = e^{-i\chi_{\mathbf{L}}(\mathbf{r}_{i-\mathbf{L}})} c_{i-\mathbf{L}} \quad \Rightarrow \quad c_{i-\mathbf{L}} = e^{i\chi_{\mathbf{L}}(\mathbf{r}_{i-\mathbf{L}})} c_i. \quad (\text{S15})$$

If one instead writes a separate boundary relation for  $-\mathbf{L}$ ,

$$c_{i-\mathbf{L}} = e^{-i\chi_{-\mathbf{L}}(\mathbf{r}_i)} c_i, \quad \chi_{-\mathbf{L}}(\mathbf{r}) = \mathbf{A}(-\mathbf{L}) \cdot \mathbf{r}. \quad (\text{S16})$$

Using  $\mathbf{r}_{i-\mathbf{L}} = \mathbf{r}_i - \mathbf{L}$  and  $\mathbf{A}(-\mathbf{L}) = -\mathbf{A}(\mathbf{L})$ , we find

$$e^{i\chi_{\mathbf{L}}(\mathbf{r}_{i-\mathbf{L}})} = e^{+i\mathbf{A}(\mathbf{L}) \cdot (\mathbf{r}_i - \mathbf{L})} = e^{+i\mathbf{A}(\mathbf{L}) \cdot \mathbf{r}_i} e^{-i\mathbf{A}(\mathbf{L}) \cdot \mathbf{L}}, \quad (\text{S17})$$

whereas

$$e^{-i\chi_{-\mathbf{L}}(\mathbf{r}_i)} = e^{-i\mathbf{A}(-\mathbf{L}) \cdot \mathbf{r}_i} = e^{+i\mathbf{A}(\mathbf{L}) \cdot \mathbf{r}_i}. \quad (\text{S18})$$

Thus, Eq. (S15) and Eq. (S16) differ by a constant factor  $\exp[-i\mathbf{A}(\mathbf{L}) \cdot \mathbf{L}]$  and correspond to different conventions.

It is convenient to write Eq. (S14) in a symmetric “mid-point” form:

$$c_i = c_{i+\mathbf{L}} \exp\left(i \mathbf{A}(\mathbf{L}) \cdot \frac{\mathbf{r}_i + \mathbf{r}_{i+\mathbf{L}}}{2}\right), \quad (\text{S19})$$

which differs from Eq. (S14) only by an  $i$ -independent constant phase factor  $\exp(\frac{i}{2}\mathbf{A}(\mathbf{L}) \cdot \mathbf{L})$  (since  $\mathbf{r}_{i+\mathbf{L}} = \mathbf{r}_i + \mathbf{L}$ ). This constant does not affect any local gauge-invariant quantity. The practical advantage of this convention is that it treats  $\pm\mathbf{L}$  in a manifestly symmetric way, reducing sign mistakes when implementing the folding-back procedure for bonds that cross the boundary in either direction. Specifically, from Eq. (S19), by replacing  $i \rightarrow i - \mathbf{L}$ ,

$$c_{i-\mathbf{L}} = c_i \exp\left(i \mathbf{A}(\mathbf{L}) \cdot \frac{\mathbf{r}_{i-\mathbf{L}} + \mathbf{r}_i}{2}\right). \quad (\text{S20})$$

Therefore, together with Eq. (S19), we write

$$c_i = c_{i \pm \mathbf{L}} \exp\left(i \mathbf{A}(\pm\mathbf{L}) \cdot \frac{\mathbf{r}_i + \mathbf{r}_{i \pm \mathbf{L}}}{2}\right), \quad (\text{S21})$$

which is convenient and avoids bookkeeping ambiguities when folding sites back into the cluster.

## II. Translation Symmetry

At the mean-field level, the magnetic unit cell of the staggered- $(\pi, 0)$  spinon ansatz contains two primitive rhombic unit cells. Nevertheless, this doubled unit cell is commensurate with the finite clusters used in this work: since we always take an even number of sites along both primitive directions, the magnetic unit cell can be chosen to extend only along one primitive direction (a  $2 \times 1$  supercell in units of primitive rhombi), while remaining primitive along the other. In this situation, for each primitive translation direction one can choose a gauge in which the corresponding translation is explicitly realized in the mean-field ansatz. Since the Gutzwiller projection is gauge invariant, the resulting projected spin state is translationally invariant under both primitive translations.

The same commensurability condition holds for all flux values considered in this work (except for the additional global flux insertion used only in evaluating the monopole matrix element). In particular, one can choose a magnetic unit cell that is primitive along a given direction and adopt a gauge in which translation symmetry along that direction is explicit in the mean-field ansatz. Therefore, the projected state is translationally invariant, and any gauge-invariant correlator such as  $C_{ij}^\perp$  depends only on the relative displacement  $\mathbf{r}_i - \mathbf{r}_j$ .

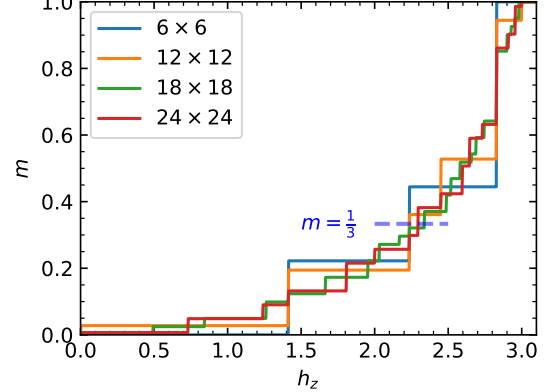


FIG. S1. Magnetization  $m$  as a function of the Zeeman field  $h_z$  for the staggered  $\pi$ -flux spinon Hamiltonian with zero net flux ( $\phi = 0$ ) for various system sizes. The dashed line indicates a target magnetization  $m = 1/3$ .

## III. Achievable Magnetization

We generate a finite magnetization by occupying  $N_\uparrow$  and  $N_\downarrow$  single-particle orbitals of the spinon Hamiltonian. To obtain a well-defined Slater-determinant wave function, one would ideally impose a closed-shell condition in each spin sector. However, for finite-size systems the single-particle spectrum of Eq. (9) typically exhibits degeneracies within each spin sector, which constrains the accessible values of  $(N_\uparrow, N_\downarrow)$ . A uniform flux can partially resolve this issue: Chern gaps open that are robust against finite-size effects. Fillings up to a Chern gap then correspond to a well-defined wave function for all system sizes, and the associated magnetization  $m$  is available on every lattice. By contrast, for  $\phi = 0$  there is no Chern gap, and the accessible magnetization values form a discrete set for any finite system.

Fig. S1 shows the magnetization  $m$  as a function of the Zeeman field  $h_z$  for the staggered  $\pi$ -flux spinon Hamiltonian. Specifically, we add a term

$$-h_z \sum_i (f_{i,\uparrow}^\dagger f_{i,\uparrow} - f_{i,\downarrow}^\dagger f_{i,\downarrow}) \quad (\text{S22})$$

to Eq. (9), diagonalize the resulting spinon Hamiltonian, fill the  $N$  lowest-energy orbitals, and compute the corresponding magnetization. The resulting  $m(h_z)$  curve exhibits magnetization plateaus, i.e.,  $m$  changes in discrete steps as  $h_z$  is varied, and these steps become finer, so that  $m(h_z)$  approaches a smooth function, as the system size increases. In practice, we need to choose a magnetization value close to the target level for meaningful comparison. For example, when we compare the  $|C| = 1$  Landau-level state at  $m = 1/3$  in Fig. 2(e) with the Fermi-pocket state at  $\phi = 0$ , we choose the plateau at  $m = 26/81$  in Fig. 2(c), which is the closest accessible magnetization to  $m = 1/3$  on the  $18 \times 18$  lattice.

#### IV. Spin Chirality and $\mathcal{R}$

Given three sites  $i, j, k$ , we define the spin chirality (with  $\varepsilon_{xyz} = \varepsilon_{yzx} = \varepsilon_{zxy} = +1$ ) as

$$\chi_{ijk} = \langle \vec{S}_i \cdot (\vec{S}_j \times \vec{S}_k) \rangle = \epsilon^{\alpha\beta\gamma} \langle S_i^\alpha S_j^\beta S_k^\gamma \rangle \quad (\text{S23})$$

$$= \langle (S_i^x S_j^y - S_i^y S_j^x) S_k^z \rangle + \langle S_i^y S_j^z S_k^x - S_i^x S_j^z S_k^y \rangle + \langle S_i^z (S_j^x S_k^y - S_j^y S_k^x) \rangle. \quad (\text{S24})$$

Using  $S^x = (S^+ + S^-)/2$  and  $S^y = -i(S^+ - S^-)/2$ , we obtain the identity  $S_i^x S_j^y - S_i^y S_j^x = i(S_i^+ S_j^- - S_i^- S_j^+)/2$ , which we use to evaluate  $\chi_{ijk}$  in Eq. (S24), i.e. the numerator of  $\mathcal{R}$ .

The denominator of  $\mathcal{R}$  is defined as the disconnected (one-point  $\times$  two-point) contribution of Eq. S24. In our variational states  $\langle S^\pm \rangle = 0$ , and the uniform longitudinal moment per site is  $\langle S_0^z \rangle = \frac{(N_\uparrow - N_\downarrow)}{N} \frac{1}{2} = m/2$ , which gives

$$\begin{aligned} & \langle S_i^x S_j^y - S_i^y S_j^x \rangle \langle S_k^z \rangle + \langle S_i^y S_k^x - S_i^x S_k^y \rangle \langle S_j^z \rangle \\ & + \langle S_i^z \rangle \langle S_j^x S_k^y - S_j^y S_k^x \rangle \\ & = \frac{im}{4} \left( \langle S_j^+ S_k^- \rangle - \langle S_j^- S_k^+ \rangle + \langle S_k^+ S_i^- \rangle - \langle S_k^- S_i^+ \rangle \right. \\ & \left. + \langle S_i^+ S_j^- \rangle - \langle S_i^- S_j^+ \rangle \right). \end{aligned} \quad (\text{S25})$$

#### V. Error Analysis

Error bars, when shown, indicate the standard error, estimated either from the fluctuations across independent Monte Carlo bins or using a jackknife analysis. No error bars are shown for the magnitudes  $|\langle S_i^+ \rangle_{\text{mono}}|$ ,  $|\langle S_i^+ S_j^+ \rangle_{\text{mono}}|$ , and  $|\langle S_i^+ S_j^+ S_k^- S_l^- + S_i^- S_j^- S_k^+ S_l^+ \rangle|$ : the plotted quantity is obtained by first averaging the complex quantity over Monte Carlo bins, then taking the absolute value, and finally averaging over sites or bonds.

#### VI. Supplementary Figures

In Fig. S2, we show the flux dependence of the variational energy for the  $J_{\text{NN}}-J_{\text{NNN}}$  model with  $J_{\text{NNNN}}/J_{\text{NN}} = 1/8$ . The behavior is similar to the  $J_{\text{NN}}$ -only case shown in Fig. 1 of the main text.

Figure S3 replots the same data as Fig. 3 on log-log axes, providing a complementary visualization of the scaling conclusions in Fig. 3. In Fig. S3(a), the  $|C| = 1$  states show an approximately linear dependence of  $\log(C^\perp(\mathbf{q} = K)/N)$  vs  $\log(1/N)$ , with slopes close to  $1/2$  over the accessible sizes. This scaling is consistent with  $C^\perp(\mathbf{q} = K)/N \sim N^{-1/2}$ , i.e., an in-plane correlation function decaying roughly as  $1/r$ . At smaller magnetizations the fitted slope is slightly larger than  $1/2$ , indicating a somewhat faster decay. For the  $|C| = 2$  state, the

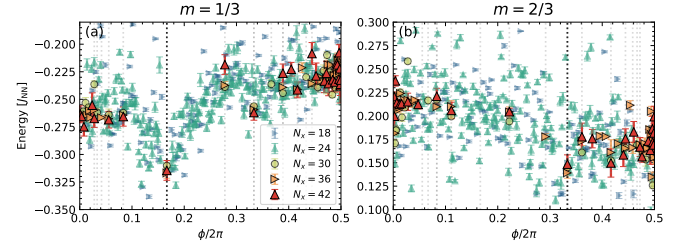


FIG. S2. Variational energies per site of the Heisenberg model including nearest neighbour interaction  $J_{\text{NNNN}}/J_{\text{NN}} = 1/8$  as a function of  $\phi$  at magnetizations  $m = 1/3$  and  $m = 2/3$ , respectively.

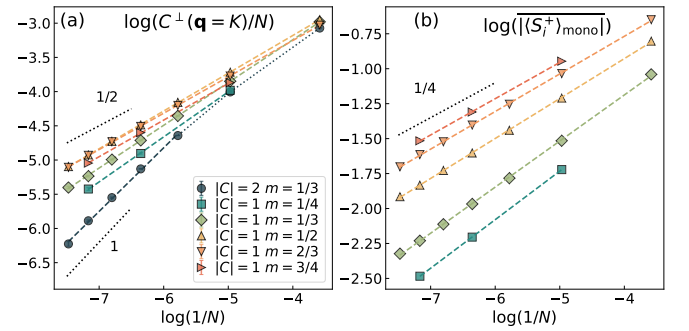


FIG. S3. Log-log scaling using the data in Fig. 3. (a)  $\log(C^\perp(\mathbf{q} = K)/N)$  vs  $\log(1/N)$ . (b)  $\log(|\langle S_i^+ \rangle_{\text{mono}}|)$  vs  $\log(1/N)$ . Dashed lines are linear fits. In (a), the  $|C| = 2$  dataset shows a clear small-size deviation (points connected by a dotted guide). Reference lines with slopes  $1/2$  and  $1$  are shown in (a), and slope  $1/4$  in (b).

smallest sizes visibly deviate from the asymptotic trend. Fitting the larger sizes gives a slope close to  $1$ , consistent with  $C^\perp(\mathbf{q} = K)/N \sim N^{-1}$  and hence short-range (summable) correlations. In Fig. S3(b),  $\log(|\langle S_i^+ \rangle_{\text{mono}}|)$  for the  $|C| = 1$  states scales approximately as  $N^{-1/4}$  (slope  $\approx 1/4$ ), compatible with the behavior in (a). The lowest magnetizations again show mild deviations from the reference slope.

Fig. S4 shows the magnitude of the transverse spin correlator  $|C_{ij}^\perp|$  as a function of distance for different Landau-level states. For  $|C| = 1$ ,  $|C_{ij}^\perp|$  is larger than for  $|C| = 2$  at comparable distances, especially at long distances, indicating more extensive transverse  $120^\circ$  correlations in the  $|C| = 1$  state.

Fig. S5 shows the finite-size behavior of  $|\chi|$  and  $\mathcal{R}$ ; both observables exhibit minimal size dependence.

Fig. S6 shows that the magnitude of the monopole matrix element  $\langle S_i^+ S_j^+ \rangle_{\text{mono}}$  for a  $|C| = 2$  Landau-level state is not largest at short separations, unlike a conventional bounded local quadrupolar order parameter, which one may expect to peak at short distance and then decay. Instead, it increases with distance and saturates into a nearly distance-independent plateau at large separations.

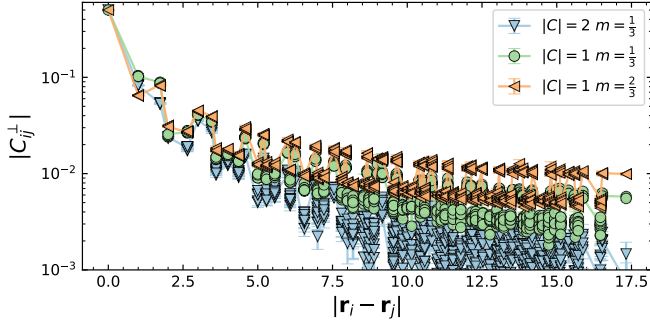


FIG. S4. Magnitude of the transverse spin correlator  $|C_{ij}^\perp|$  as a function of distance on a  $30 \times 30$  lattice for various Landau-level states. Exploiting translational invariance and periodic boundary conditions,  $|\mathbf{r}_i - \mathbf{r}_j|$  is taken as the shortest distance on the torus.

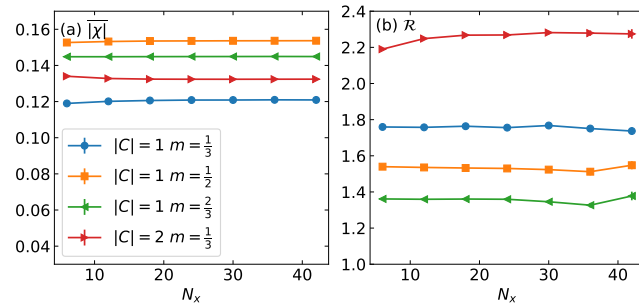


FIG. S5. Finite-size behavior of  $\overline{|\chi|}$  (a) and  $\mathcal{R}$  (b) at representative parameters, using square clusters with  $N_x = N_y$ .

Fig. S7 shows the phases of the nearest-neighbour four-spin correlation functions  $\langle S_i^+ S_j^+ S_k^- S_l^- \rangle$  and  $\langle S_i^- S_j^- S_k^+ S_l^+ \rangle$ . Consistent with  $\langle S_i^+ S_j^+ \rangle_{\text{mono}}$ , both correlators exhibit the same three-sublattice structure.

## VII. Parent Hamiltonian Search

We use the correlation-matrix method of Ref. [24] to test whether a Gutzwiller-projected state  $|\psi\rangle$  admits a local parent Hamiltonian built from short-range Heisenberg exchanges. As candidate terms we take

$$\hat{O}_m \equiv \sum_{\langle ij \rangle_m} \vec{S}_i \cdot \vec{S}_j, \quad m = 1, 2, \dots, 5, \quad (\text{S26})$$

where  $\langle ij \rangle_m$  denotes  $m$ -th-nearest-neighbor bonds on the lattice (nearest through 5th neighbor). We form the connected covariance (correlation) matrix of these operators,

$$C_{mn} \equiv \langle \delta \hat{O}_m \delta \hat{O}_n \rangle, \quad \delta \hat{O}_m \equiv \hat{O}_m - \langle \hat{O}_m \rangle, \quad (\text{S27})$$

which is positive semidefinite by construction.

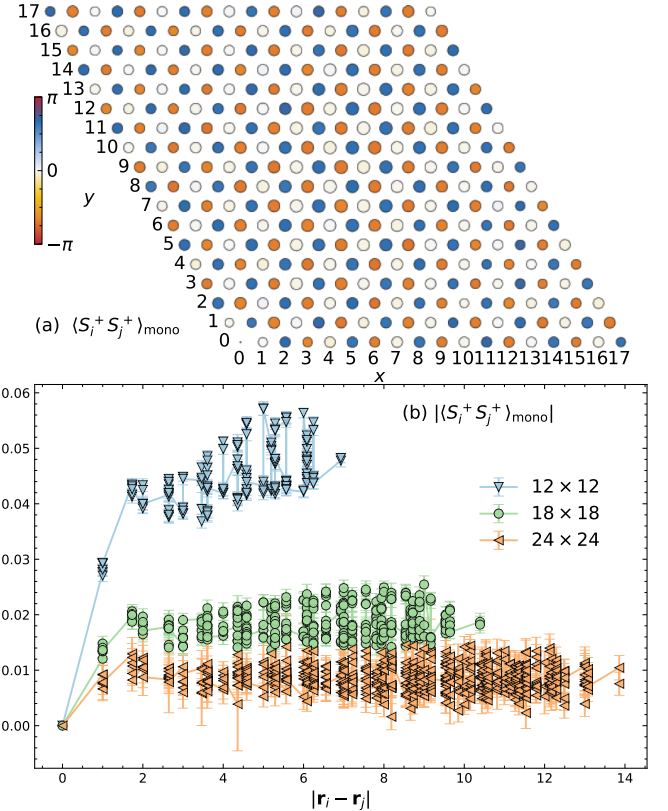


FIG. S6. (a) Spatial structure of the monopole matrix element  $\langle S_i^+ S_j^+ \rangle_{\text{mono}}$  for the  $|C| = 2$  state at  $m = 1/3$  on an  $18 \times 18$  lattice, with site  $i$  fixed at  $(0, 0)$ . Marker size encodes the magnitude and color encodes the phase, normalized by the value at  $j = (1, 0)$ . (b) Magnitude of the same quantity,  $|\langle S_i^+ S_j^+ \rangle_{\text{mono}}|$ , for  $i = (0, 0)$  as a function of the distance between sites  $i$  and  $j$  for different lattice sizes. The distance  $|\mathbf{r}_i - \mathbf{r}_j|$  is defined as the shortest distance on the torus.

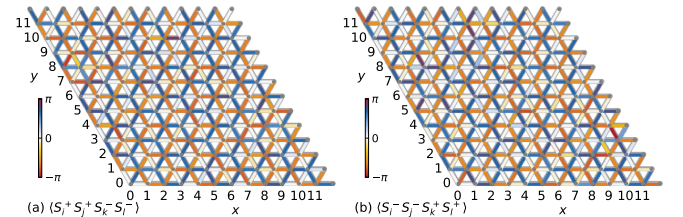


FIG. S7. Phase patterns of the nearest-neighbour four-spin correlators (a)  $\langle S_i^+ S_j^+ S_k^- S_l^- \rangle$  and (b)  $\langle S_i^- S_j^- S_k^+ S_l^+ \rangle$  for the  $|C| = 2$  state at  $m = 1/3$  on a  $12 \times 12$  lattice. The pairs  $(i, j)$  and  $(k, l)$  each form nearest-neighbour bonds, with  $(k, l) = ((1, 0), (0, 0))$  chosen as a reference bond.

We restrict attention to Hamiltonians in the span of  $\{\hat{O}_m\}$ ,

$$H(\gamma) \equiv J_0 \sum_m \gamma_m \hat{O}_m, \quad (\text{S28})$$

with an arbitrary overall scale  $J_0$ . The energy variance in  $|\psi\rangle$  reads

$$\text{Var}_\psi[H] = \left\langle (H - \langle H \rangle)^2 \right\rangle = J_0^2 \sum_{mn} \gamma_m C_{mn} \gamma_n = J_0^2 \gamma^\top C \gamma. \quad (\text{S29})$$

Hence  $|\psi\rangle$  is an exact eigenstate of some  $H(\gamma)$  in this span iff  $\text{Var}_\psi[H] = 0$ , which (since  $C \succeq 0$ ) holds exactly when

$$C \gamma = 0. \quad (\text{S30})$$

Any null vector  $\gamma$  of  $C$  therefore specifies a parent Hamiltonian within the chosen basis (up to normalization).

In practice we work with a truncated, finite-range basis and with Monte-Carlo estimates of correlators, so an exact zero mode is not expected. However, the true parent Hamiltonian could still be “almost local.” We therefore diagonalize  $C$  and take the eigenvector  $v_{\min}$  associated with the smallest eigenvalue  $N\lambda_{\min}$  (with  $\|v_{\min}\|_2 = 1$ ) as defining the best-fit local parent Hamiltonian within the span  $\{\hat{O}_m\}$ . The value of  $J_0^2 \lambda_{\min}$  quantifies the minimal attainable energy variance (normalized by size) and serves as a metric for how closely  $|\psi\rangle$  can be an eigenstate of a local Heisenberg-type Hamiltonian of this form. In other words, we interpret  $\lambda_{\min}$  and  $v_{\min}$  comparatively across candidate states and as we enlarge the operator set: smaller  $\lambda_{\min}$  indicates a more nearly local parent within this basis, while the components of  $v_{\min}$  indicate which exchange channels are most favored to stabilize  $|\psi\rangle$ . All error bars for  $\lambda_{\min}$  and  $v_{\min}$  represent one standard error estimated via delete-one jackknife over Monte Carlo bins.

Fig. S8 summarizes the correlation-matrix results for five representative parameter choices. For each state and system size we increase the maximal interaction range  $R$  from nearest-neighbor ( $R = 1$ ) to fifth-neighbor ( $R = 5$ ) bonds in the operator set  $\{\hat{O}_m\}$ , and determine the minimal variance  $\lambda_{\min}(R)$  together with the corresponding eigenvector  $v_{\min}(R)$ . As shown in the left panels,  $\lambda_{\min}$  decreases systematically as  $R$  is enlarged, as expected when the space of admissible Hamiltonians is expanded. The right panels display the associated coupling profiles: for each  $R$  and lattice size we plot the components  $\gamma_m$  of  $v_{\min}(R)$  as a function of bond range  $m$ , which we interpret as the reconstructed “parent” Hamiltonian within the chosen basis. Since  $S_{\text{tot}}^z$  is conserved and all states are exact eigenstates of  $S_{\text{tot}}^z$ , adding a uniform Zeeman term to the inferred parent Hamiltonian would not change the energy variance and is therefore not constrained by this analysis.

As the allowed range increases, the reconstructed Hamiltonians extend to longer-distance couplings but remain strongly dominated by short-range exchanges, with sizeable nearest- and next-nearest-neighbor components and much smaller further-neighbor terms. At  $m = 1/3$

[Figs. S8 (b,d)], the  $|C| = 1$  and  $|C| = 2$  Landau-level states yield broadly similar patterns of  $\gamma_m$ , and these profiles are also qualitatively close to those obtained for the zero-flux Fermi-pocket states at comparable magnetizations [Fig. S8 (j)]. For  $m = 2/3$  [Figs. S8 (e,f)],  $\lambda_{\min}$  is smallest among all cases, and the reconstructed coupling profiles show visibly larger error bars and a stronger sensitivity to  $R$ , consistent with near-flat directions in coupling space. In this regime a family of nearby local Hamiltonians can achieve comparably small  $\lambda_{\min}$ , making the parent Hamiltonian less tightly constrained.

Finally, when we restrict to  $R = 2$  for the zero-field  $m = 0$  state [Fig. S8(h)], the optimized ratio of next-nearest- to nearest-neighbor couplings is  $\gamma_2/\gamma_1 \approx 0.18$ . Interpreting this restricted fit as an effective estimate of the optimal  $J_{\text{NNN}}/J_{\text{NN}}$  ratio for stabilizing the DSL within a nearest- and next-nearest-neighbor Heisenberg model, this value lies close to the upper edge of the spin-liquid window inferred in previous numerical studies of the triangular-lattice  $J_1$ - $J_2$  model, including VMC [9], DMRG [8, 25], and CCM [26], which identify a spin-liquid regime without long-range magnetic order. Thus, our parent-Hamiltonian reconstruction for this trial state is broadly consistent with these independent estimates.

## VIII. Symmetry Analysis

We here show a symmetry-based construction of observables for the field-induced flux state. To this end, we note that at  $h = 0$ , the DSL exhibits both a spin-1/2 time-reversal symmetry (TRS)  $\mathcal{T} = i\sigma^y \mathcal{K}$  with  $\mathcal{K}$  denoting complex conjugation, and a spinless TRS  $\mathcal{T}' = \mathcal{K}$ , i.e. it is possible to find a gauge in which the parton Hamiltonian is real. Applying a finite Zeeman field  $h^z \neq 0$  explicitly breaks time-reversal symmetry  $\mathcal{T}$ , but  $\mathcal{T}'$  need not be broken: for example, the parton Hamiltonian for a Fermi pocket-state will be invariant under  $\mathcal{T}'$ .

An explicit inspection shows that a non-trivial flux  $\Phi \neq 0, \pi$  in a triangular plaquette breaks a vertical mirror symmetry  $M_x : (x, y) \rightarrow (-x, y)$  as it reverses the flux  $\Phi \rightarrow -\Phi$ . Here  $\Phi$  is the flux per triangular plaquette; in our convention  $\phi = 2\Phi$  is the flux per rhombic unit cell.

We further note that the parton Hamiltonian for the Landau-level state with flux  $[\Phi, \pi + \Phi]$  in  $\Delta, \nabla$ -triangles appears to also break a horizontal reflection symmetry  $M_y : (x, y) \rightarrow (x, -y)$  (which interchanges  $\Delta$  and  $\nabla$ -triangles) even in the absence of a net flux,  $\Phi = 0$ , but we point out that this is a *projective symmetry*: we may perform a  $SU(2)$  gauge transformation  $G : f_{i,\uparrow} \rightarrow f_{i,\downarrow}^\dagger$  and  $G : f_{i,\downarrow} \rightarrow -f_{i,\uparrow}^\dagger$  which leaves all spin operators (and, thus, also all physical observables)  $\tilde{S}_i = 1/2 \sum_{\alpha,\beta} f_{\alpha,i}^\dagger \vec{\sigma}_{\alpha\beta} f_{\beta,i}$  invariant, and changes the flux per triangle plaquette by  $\pi$ . Therefore, a state with flux  $[\Phi, \pi + \Phi]$  is gauge-equivalent to  $[\pi + \Phi, \Phi]$ , and the Landau-level state is symmetric under *physical*  $M_y$ .

reflection symmetries.

Now, consider a triangle with points  $\mathbf{r}$ ,  $\mathbf{r} + \mathbf{n}_1$  and  $\mathbf{r} + \mathbf{n}_2$  where  $\mathbf{n}_1 = (1, 0)$  and  $\mathbf{n}_2 = (1/2, \sqrt{3}/2)$ . We write down the most general expression  $\mathcal{O}_3 = \sum_{\alpha, \beta, \gamma \in \{+, -, z\}} (f_{\alpha\beta\gamma} + ig_{\alpha\beta\gamma}) S_{\mathbf{r}}^{\alpha} S_{\mathbf{r} + \mathbf{n}_1}^{\beta} S_{\mathbf{r} + \mathbf{n}_2}^{\gamma}$ . It is convenient to work with  $S^+ = S^x + iS^y$  and  $S^- = S^x - iS^y$  which have the following transformation properties:

$$\mathcal{T} : S^{\pm} \rightarrow -S^{\mp}, \mathcal{T}' : S^{\pm} \rightarrow S^{\pm} \quad \text{and} \quad R_z(\varphi) : S^{\pm} \rightarrow e^{\pm i\varphi} S^{\pm} \quad (\text{S31})$$

We now impose 1) hermiticity, 2) invariance under  $U(1)_z$  spin rotations, i.e.  $R_z(\varphi)$ , and 3) odd-ness under  $\mathcal{T}$ . Finally, we impose odd-ness under  $M_x$  which maps the triangle unto itself (but interchanges  $\mathbf{r}$  and  $\mathbf{r} + \mathbf{n}_1$ ), and its symmetry-equivalent version which interchanges  $\mathbf{r} + \mathbf{n}_1$  and  $\mathbf{r} + \mathbf{n}_2$ ). It can be shown that the only observable that is compatible with these requirements is the scalar spin chirality  $\chi_{\mathbf{r}, \mathbf{r} + \mathbf{n}_1, \mathbf{r} + \mathbf{n}_2} = \vec{S}_{\mathbf{r}} \cdot (\vec{S}_{\mathbf{r} + \mathbf{n}_1} \times \vec{S}_{\mathbf{r} + \mathbf{n}_2})$ .

Now, finally, we further impose  $M_y$ . This fixes a spatial pattern for the chirality: Consider  $\langle \vec{S}_{\mathbf{r}} \cdot (\vec{S}_{\mathbf{r} + \mathbf{n}_1} \times \vec{S}_{\mathbf{r} + \mathbf{n}_2}) \rangle = \chi_{\Delta}$  and  $\langle \vec{S}_{\mathbf{r}} \cdot (\vec{S}_{\mathbf{r} + \mathbf{n}_1 - \mathbf{n}_2} \times \vec{S}_{\mathbf{r} + \mathbf{n}_1}) \rangle = \chi_{\nabla}$ . Applying  $M_y$ , we have

$$\begin{aligned} & \vec{S}_{\mathbf{r}} \cdot (\vec{S}_{\mathbf{r} + \mathbf{n}_1} \times \vec{S}_{\mathbf{r} + \mathbf{n}_2}) \\ & \rightarrow \vec{S}_{\mathbf{r}} \cdot (\vec{S}_{\mathbf{r} + \mathbf{n}_1} \times \vec{S}_{\mathbf{r} - \mathbf{n}_2 + \mathbf{n}_1}) = -\vec{S}_{\mathbf{r}} \cdot (\vec{S}_{\mathbf{r} - \mathbf{n}_2 + \mathbf{n}_1} \times \vec{S}_{\mathbf{r} + \mathbf{n}_1}) \end{aligned} \quad (\text{S32})$$

and therefore we see that  $\chi_{\Delta} = -\chi_{\nabla}$ . We conclude that in the Landau-level state with the prescribed symmetries, the spin chirality must be staggered.

## IX. Scalar Spin Chirality in Classical and Quantum Limits

Below, we compare the scalar spin chirality measured with respect to the Gutzwiller-projected spinon Landau level state with two limiting cases: the classical (mean-field) limit and the maximal spin chirality possible for three spins.

### A. Classical Limit

As a point of comparison, we consider a classical arrangement of spins on the triangular lattice which features (1) in-plane  $120^\circ$  antiferromagnetic order and (2)

a finite magnetization. This is commonly referred to as a “umbrella” or “cone” state. Formally, for  $S = 1/2$ , such a state is described by a product-state wavefunction where on each site  $i$  the spin-1/2 degree of freedom is in a coherent state  $|\psi_i\rangle = |\vec{n}_i\rangle$  parametrized by a unit vector  $\vec{n}$  such that  $\langle \psi_i | \vec{S}_i | \psi_i \rangle = S\vec{n}$ . If we use standard polar coordinates for  $\vec{n}$ , this then reduces to the Bloch representation  $|\psi_i\rangle = \cos \theta/2 | \uparrow \rangle + e^{i\varphi} \sin \theta/2 | \downarrow \rangle$  with  $\varphi \in [0, 2\pi)$  and  $\theta \in [0, \pi]$ . For the three-sublattice state, we consider without loss of generality the configuration (any global in-plane rotation  $\varphi \rightarrow \varphi + \text{const}$  will leave the chirality invariant)

$$\vec{n}_j = \begin{pmatrix} \cos(2j\pi/3) \sin \theta \\ \sin(2j\pi/3) \sin \theta \\ \cos \theta \end{pmatrix}, \quad (\text{S33})$$

where  $j = 0, 1, 2$  on  $A, B, C$  sublattices. The angle  $\theta$  is determined by the magnetization sector to be considered, labelled by the density  $m = M/N = (SN)^{-1} \sum_i S_i^z$  with  $S = 1/2$ .

With respect to above product-state wavefunction, we then compute the scalar-spin chirality as

$$\begin{aligned} \langle \vec{S}_i \cdot (\vec{S}_j \times \vec{S}_k) \rangle &= \langle \vec{S}_i \rangle \cdot (\langle \vec{S}_j \rangle \times \langle \vec{S}_k \rangle) \\ &= \frac{3\sqrt{3}}{2} S^3 m (1 - m^2) \end{aligned} \quad (\text{S34})$$

where we have used  $\sin^2 \theta = 1 - \cos^2 \theta = 1 - m^2$ , and we should plug in  $S = 1/2$ . The result is shown graphically as a function of  $m$  in Fig. 4(b).

### B. Quantum Limit

To find the maximum possible value that the scalar spin chirality can attain in the quantum theory, we may consider three spin-1/2 degrees of freedom on a triangle and diagonalize  $\vec{S}_1 \cdot (\vec{S}_2 \times \vec{S}_3)$ . We find the eigenvalues  $-\sqrt{3}/4$  (multiplicity 2),  $\sqrt{3}/4$  (multiplicity 2) and 0 (multiplicity 4), thereby bounding  $|\chi_{ijk}| \leq \sqrt{3}/4$ . We stress that this value will be reduced in any lattice system as every pair of two spins contributes to the spin chirality on two adjacent triangular plaquettes. Since  $[\chi_{ijk}, \chi_{lji}] \neq 0$  for  $k \neq l$ , the chiralities on two adjacent plaquettes cannot be simultaneously maximized.

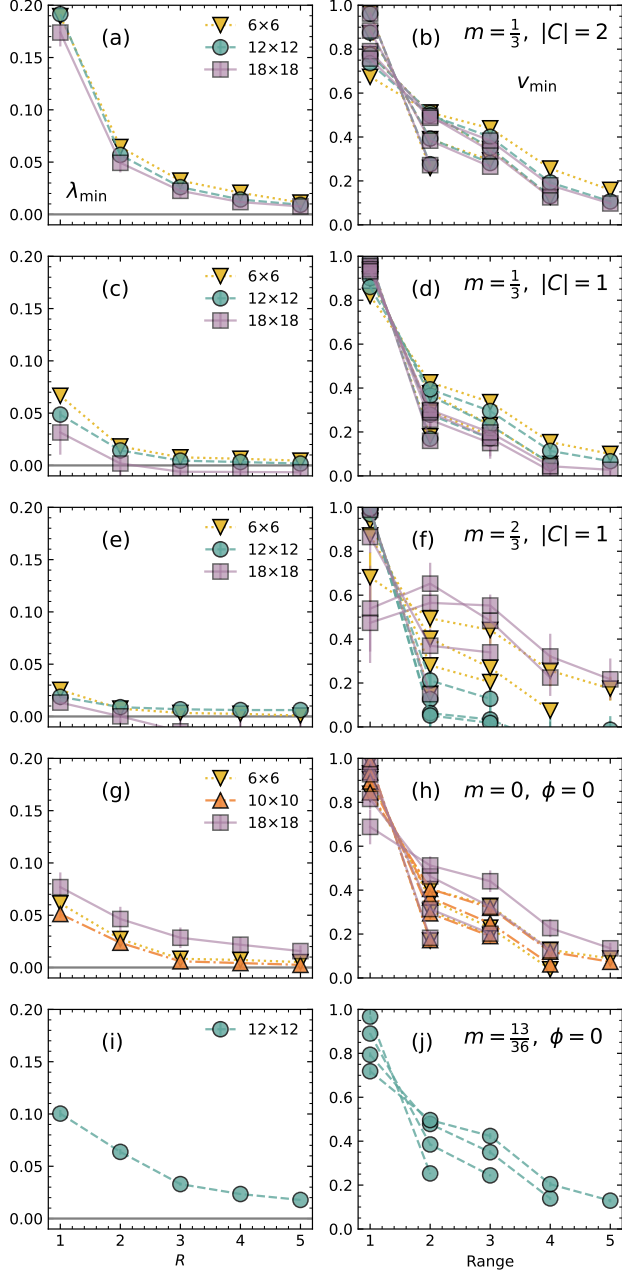


FIG. S8. Correlation-matrix diagnosis of local parent Hamiltonians. For each state and system size we compute the covariance matrix  $C_{mn}$  of Heisenberg exchanges  $\hat{O}_m = \sum_{\langle ij \rangle_m} \vec{S}_i \cdot \vec{S}_j$  up to a maximum bond range  $R$  and consider normalized Hamiltonians  $H(\gamma) = J_0 \sum_m \gamma_m \hat{O}_m$  with  $\|\gamma\|_2 = 1$ . (a,c,e,g,i) Smallest eigenvalue  $\lambda_{\min}$  of  $C/N$ , which gives the minimal energy variance (normalized by  $J_0^2$ ) within this subspace, as a function of the maximum range  $R$  ( $R = 1$  for nearest-neighbor couplings,  $\dots$ ,  $R = 5$  for fifth neighbors). (b,d,f,h,j) Corresponding normalized eigenvectors  $v_{\min}(R)$ , showing the profile of optimal couplings  $\gamma_m$  versus bond range  $m$ . For each lattice size, five curves are shown, obtained for  $R = 1, \dots, 5$ ; each curve terminates at its own maximal range. Different marker shapes and line styles denote different lattice sizes as indicated in the legends. Rows correspond to different magnetizations  $M$  and flux choices, as labeled in the right-hand panels.